Rock Mechanics and Rock Engineering (2020) 53:4429–4447
https://doi.org/10.1007/s00603-020-02074-7

ORIGINAL PAPER

# Experimental and Numerical Investigations of the Dynamic Permeability Evolution of a Fracture in Granite During Shearing Under Different Normal Stress Conditions

Haimeng Shen[1,3] · Qiang Zhang[2,4] · Qi Li[1] · Xiaochun Li[1] · Lu Shi[1] · Nao Shen[1,3]

Received: 19 September 2019 / Accepted: 18 February 2020 / Published online: 2 March 2020


## Abstract

The dynamic permeability evolution of a fracture is a key scientific problem for fluid flows in rock masses within engineering systems. Understanding the dynamic permeability evolution and its mechanism is conducive to design and operation engineering. The dynamic permeability evolution of a rough granite fracture was revealed by laboratory experiments and numerical models. The permeability evolution of six fractured samples with rough fractures were monitored under 1.9–20 MPa effective normal stresses. The results show that the shearing process significantly affects the permeability and that the variation trend of the permeability depends on the magnitude of the effective normal stress. Under effective normal stresses of 1.9–5 MPa, the permeability is first significantly enhanced and then decreased by shearing. When effective normal stresses of more than 5 MPa are applied, the permeability only shows a decreasing trend. A high effective normal stress not only limits the dilatancy of a fracture but also enhances the formation of fault gouges. The mechanism of the dynamic permeability evolution was revealed by numerical simulations based on the discrete element method. The shearing mechanism includes the sliding mechanism and shearing mechanism. Under a low normal stress, first, the sliding mechanism is dominant and decreases the contact area, which is conducive to establishing a flow channel and increases the permeability. Then, the shearing mechanism becomes increasingly impactful, causing the contact area to increase and the permeability to decrease. Under a high normal stress, the sliding and shearing mechanisms are always engaged, which generates many wear products and reduces the permeability.

**Keywords** Joints · Shear-flow coupling · PFC · Smooth joint model · Contact area · Shear mechanism

## Abbreviations

| | |
|---|---|
| $A$ | Area of contact |
| Ar | Relative contact area |
| $E_c$ | Effective modulus of both the particle and parallel bond |
| $F$ | Contact force |
| $F_s^{\mu}$ | Greatest value of the shear force at the SJ contact |
| $F_s^*$ | Updated shear force at the SJ contact |
| $F_n$ | Normal component of the contact force |
| $F_s$ | Shear component of the contact force |
| JRC | Joint roughness coefficient |
| $P_p$ | Pore pressure |
| $U$ | Relative displacement |
| $U_n$ | Normal component of the relative displacement |
| $U_s$ | Shear component of the relative displacement |
| $R$ | Radius of SJ |
| $R_i$ | Radius of particle $i$ |
| $T$ | Tensile strength |
| SJ | Smooth joint |
| $Z_2$ | Root mean square of the first derivative of the profile |
| $k_n$ | SJ normal stiffness |
| $k_s$ | SJ shear stiffness |
| $k$ | Permeability |
| $k_0$ | Initial permeability |

✉ Qiang Zhang
zhangqiang02016@163.com

[1] State Key Laboratory of Geomechanics and Geotechnical Engineering, Institute of Rock and Soil Mechanics, Chinese Academy of Sciences, Wuhan 430071, Hubei, China

[2] Powerchina Huadong Engineering Corporation Limited, Hangzhou 311122, Zhejiang, China

[3] University of Chinese Academy of Sciences, Beijing 100049, China

[4] Powerchina Zhejiang Huadong Engineering Consulting Corporation Limited, Hangzhou 311122, Zhejiang, China

| | |
|---|---|
| $k_{ave}$ | Average permeability |
| $k_n/k_s$ | Ratio of the normal stiffness to the shear stiffness of both the particle and parallel bond |
| $\mu$ | SJ coefficient of friction |
| $\psi$ | SJ dilation angle |
| $m$ | Number of sampling points |
| $n_j$ | Unit normal vector of the joint |
| $n_c$ | Unit normal vector of a contact |
| $r_{min}$ | Minimum particle radius |
| $r_{max}$ | Maximum particle radius |
| $y_i$ | Elevation of the sampling point |
| $\Delta$ | Increment |
| $\lambda$ | Radius multiplier of SJ |
| $\Delta x$ | Sampling interval |
| $\sigma_n$ | Normal stress |
| $\sigma_n^e$ | Effective normal stress |
| $\sigma_b$ | Tensile strength of the parallel bond |
| $c_b$ | Cohesion strength of the parallel bond |
| $\phi_b$ | Local friction angle of the parallel bond |
| $\rho$ | Particle density |

## 1 Introduction

Rock masses are composed of rocks and discontinuities, and the mechanical and hydraulic properties of rock masses are closely related to their discontinuities (Lang et al. 2016; Yeo et al. 1998). Fractures are the main pathways for fluid flow in rock masses. The hydraulic properties of fractures under normal stress and shear stress conditions are vital to oil and gas production, $CO_2$ geological storage, enhanced geothermal systems and nuclear waste disposal (Fang et al. 2017; Faoro et al. 2009; Lee and Cho 2002; Takahashi 2003). Fluid injection and tectonic stress may cause a shearing process in fractures. The fracture apertures will thereby be altered, and the contact surfaces will be damaged during shearing, leading to a permeability change in the fractured rock (Fang et al. 2017; Giwelli et al. 2016). The permeability change will affect the fluid flow within these rock masses. Understanding the dynamic permeability evolution of a fracture during shearing under high-normal stress conditions is conducive to designing and operating the abovementioned projects. The hydraulic properties of fractures in various lithology types under normal stress without shear stress have been extensively researched (Bart et al. 2004; Ji et al. 2013; Snow 1969; Stober and Bucher 2015; Witherspoon et al. 1980; Yang et al. 2017). However, the dynamic permeability evolution of a fracture during shearing has not been fully investigated, as the required experimentation is difficult and the theory is complicated. It is important to further study the dynamic permeability evolution of a fracture and to reveal the mechanism of permeability changes during shearing under normal stress and shear stress conditions.

A large number of constitutive models have been proposed to describe the effect of normal stress on the hydraulic properties of a fracture (Amadei and Illangasekare 1994; Bart et al. 2004; Ji et al. 2013; Kamali-Asl et al. 2018; Shu et al. 2019; Snow 1969; Witherspoon et al. 1980; Yang et al. 2017). However, knowledge of the dynamic hydraulic properties of a fracture during shearing is insufficient due to the limitations associated with sealing the test apparatus for shear-flow experiments (Giger et al. 2011; Yang et al. 2017). The permeability of a fracture is significantly affected by shearing (Barton et al. 1985; Esaki et al. 1999; Lee and Cho 2002). Previous experimental results showed that the permeability of a fracture was enhanced by shearing (Esaki et al. 1999; Nishiyama et al. 2014; Wang Gang 2009; Yeo et al. 1998). With increasing shear displacement, the permeability of a granite fracture was increased by two orders of magnitude. However, Giwelli et al. (2016) found that the transmissibility of a carbonate fracture was permanently decreased during shearing under a high normal stress. The permeability of a fracture decreased with increasing normal stresses because many asperities were sheared off and more gouge was produced. The normal stress magnitude is a key factor influencing the fracture permeability. Faoro et al. (2009) studied the permeability characteristics of smooth fractures in tight sandstone during shearing. Under a normal stress, the permeability of the smooth fractures decreased by two orders of magnitude after experiencing a large shear displacement. Rong et al. (2016) studied the nonlinear characteristics of transmissibility in a granite fracture via a shear flow experiment. The results showed that the nonlinear coefficient is very sensitive to the shearing process and that the fracture permeability decreases greatly with large shear displacements. Regarding granite fractures, the dynamic permeability evolution is not yet well understood. In addition, changes in the permeability of a fracture influence the shear movement of the pre-existing fracture (Fang et al. 2017; Ishibashi et al. 2016). Therefore, further investigation is needed to revealed the dynamic permeability evolution of granite fractures under normal stress and shear stress.

It is obvious that the shear behaviour is significant for the permeability of fractures. Regarding the roughness of fractures, the contact state of the fracture surfaces will change during the shear test. The connection of a fracture depends on the contact state. Additionally, many asperities on the fracture surface are sheared off during the shearing process. The wearing of the fracture surface significantly influences the fracture permeability (Fang et al. 2017). However, it is difficult to directly observe the variation of the contact state and crack generation during shear testing in laboratory experiments. Numerical simulations are regarded as a useful study method. Compared with the numerical methods based on continuum theory, the discrete element method (DEM) is a promising approach in numerical modelling for addressing

discontinuity problems and simulating crack propagation. The particle flow code PFC (Itasca Consulting Group 2014) is one of the platforms based on the DEM. In the PFC model, a rock sample is simulated as many bonded particles. The mechanical behaviour of the rock is determined by the contact model of the particles. During the shearing process, when the applied force exceeds the strength of the bond between two particles, the bond is removed, and a crack is generated. This characteristic enables the numerical method to simulate the propagation of cracks during a shear test. With this method, many researchers have investigated the shear behaviours of fractured rock masses. By analysing the whole process of shearing, researchers successfully revealed the influences of geometrical features on the shear behaviour of fractures (Asadi et al. 2012; Park and Song 2013) and studied the shear strength and asperity degradation of a fractured rock (Asadi et al. 2013b; Bahaaddini et al. 2016; Huang et al. 2014). Nevertheless, most of these studies only focused on the shear behaviour of rock joints, and the relationship between the shear mechanism and permeability has rarely been studied.

In this work, both laboratory shear-flow tests and numerical shearing tests were carried out to investigate the effects of normal conditions on the dynamic permeability evolution of a granite fracture and reveal the mechanism of permeability evolution. This paper is organised as follows: Section 2 introduces the experimental setup, including the sample preparation, test apparatus and experimental procedure. Additionally, the experimental results and the dynamic permeability evolution of a granite fracture during shearing under different effective normal stresses are presented. Section 3 mainly reports the numerical model setup, along with the description of the contact model and parameter calibration. In particular, in this section, the reasons behind permeability changes during shearing are analysed. The experimental and numerical results are discussed in Sect. 4. Section 5 summarizes the whole study.

## 2 Laboratory Shear Flow Tests Under Different Normal Conditions

### 2.1 Experimental Methods

#### 2.1.1 Sample Preparation and Apparatus

The permeability of intact granite is very low, and it can be considered impermeable when compared to the fracture permeability. The granite was quarried from Qichun County, Hubei Province, China. The components of the granite are shown in Table 1. The granite was cored from a block into cylinders with a diameter of 38 mm and a length of 70 mm. Then, the Brazilian test was employed to prefabricate a single fracture along the axis of each core, as shown Fig. 1. Afterward, the fracture surfaces were scanned using a laser scanner (3DS capture mini, USA), and a profile of each fracture surface was extracted from the scanning data. The root mean square of the first derivative of the profile ($Z_2$) and the joint roughness coefficient (JRC) were calculated based on the point data of the fracture surfaces and Eqs. (1) and (2) (Yang et al. 2001):

**Table 1** Mineral composition of the granite

| Mineral | Quartz | Albite | Orthoclase | Microcline | Muscovite |
|---|---|---|---|---|---|
| wt% | 28.64 | 33.91 | 7.55 | 21.15 | 8.75 |

$$Z_2 = \sqrt{\frac{1}{m-1}\sum_{1}^{m-1}\left(\frac{y_{i+1}-y_i}{\Delta x}\right)^2}, \tag{1}$$

$$\mathrm{JRC} = 32.69 + 32.98 \times \log_{10} Z_2. \tag{2}$$

Here, $\Delta x$ is the sampling interval, $\Delta x = 0.5$ mm, $y_i$ is the elevation of the sampling point, and $m$ is the number of sampling points. In this study, six cores were tested, and their geometric parameters are compiled in Table 2.

Pre-existing shear flow apparatuses have limitations in terms of sealing high-pressure pore fluid and measuring the low permeability of a fracture during testing. Thus, a new shear assembly that couples a fracture with high-pressure pore fluid was developed to meet the requirements of this study, as shown Fig. 2. The shear assembly coupled with a true or conventional triaxial apparatus can be used to achieve the shear flow test, providing shear stress via the axial load and normal stress through the confining pressure. In this work, a true triaxial machine located at the Institute of Rock and Soil Mechanics, Chinese Academy of Sciences, was used. The shear assembly consisted of two inverted shear blocks of type L and a bedplate with normal deformation sensors, as shown in Fig. 2b, c. The shear blocks were semi-cylinders with a cylindrical pedestal, and the missing semi-cylindrical space was filled with a silicone plug and semi-circular steel sheet to prevent sleeve tearing by the high-pressure oil. Because the Poisson's ratio value of silicon is very large ( = 0.48–0.5) and its elasticity modulus is small (approximately 2.14 MPa), a small force could cause a large deformation of the silicone. Thus, the silicone plug could not hinder the shear movement of the fracture. The transient pulse method and the constant-pressure steady-state method are alternative methods for measuring the fracture sample permeability. This testing method has three advantages under the use of high-pressure pore fluid, as follows: (1) the normal stress applied to the pre-existing fracture is always equal to the confining pressure and does not

**Fig. 1** The granite sample with a single fracture prefabricated by the Brazilian splitting test

**Table 2** The joint roughness coefficients

| Sample | Initial diameter/mm | Fractured diameter/mm | $Z_0$ | JRC |
|---|---|---|---|---|
| 1# | 38.20 × 69.65 | 38.46 × 69.68 | 0.283 | 14.62 |
| 2# | 38.18 × 69.54 | 38.50 × 69.56 | 0.264 | 13.60 |
| 3# | 38.12 × 69.43 | 38.12 × 69.43 | 0.259 | 13.35 |
| 4# | 38.17 × 69.64 | 38.43 × 69.62 | 0.245 | 12.54 |
| 5# | 38.16 × 69.74 | 38.54 × 69.72 | 0.265 | 13.17 |
| 6# | 38.12 × 69.60 | 38.38 × 69.56 | 0.251 | 12.89 |

vary with the shear displacement; (2) it is easy to seal the high-pressure pore fluid due to the presence of the higher confining pressure and sleeve; and (3) the permeability of a fracture can be measured at any shear displacement during shearing.

### 2.1.2 Experimental Procedure

The matched fractures as the object of this research, and the permeability was low (Gong Gangyan 1990). The transient method was adopted to measure the permeability of fractures under a high normal stress, and the constant-pressure steady-state method was used to test low-normal stress conditions. The aperture and the shear strength of a fracture mainly depend on the effective normal stress (Rutter and Hackston 2017; Zhang et al. 2018). Thus, the effective normal stress was adopted in this work. Four levels of effective normal stress were used to distinguish its impact on the evolution of fracture permeability. The detailed test parameters are presented in Table 3.

The experimental procedure was divided into four steps, and the detailed procedure was as follows:

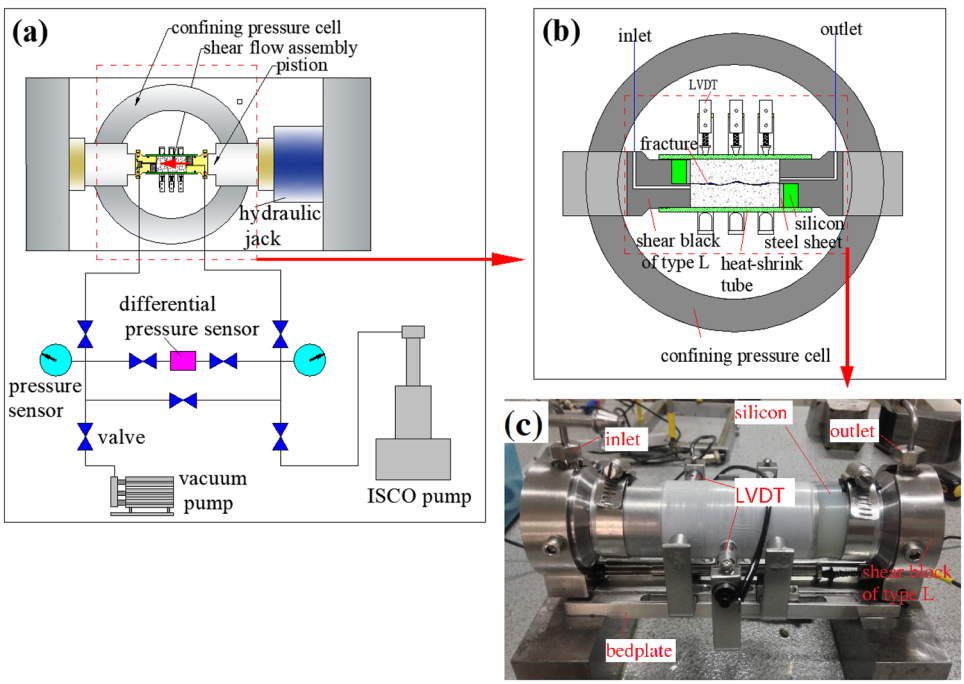


**Fig. 2** Schematic diagram of the direct shear flow system, which allows for high-pressure pore fluid: **a** the direct shear flow system; **b** the shear assembly installed into the confining cell; and **c** the shear assembly

**Table 3** The test scheme for the measurement of the fracture permeability

| Sample | Method of permeability measurement | Normal stress $\sigma_n$/MPa | Pore pressure $P_p$/MPa (fluid) | Effective normal stress $\sigma_n^e$/MPa |
|---|---|---|---|---|
| #1 | Constant pressure method | 2 | 0.1 (water) | 1.9 |
| #2 | | 2 | 0.1 (water) | 1.9 |
| #3 | Transient method | 10 | 5 (nitrogen) | 5 |
| #4 | | 15 | 5 (nitrogen) | 10 |
| #5 | | 20 | 5 (nitrogen) | 15 |
| #6 | | 25 | 5 (nitrogen) | 20 |

(1) Sample preparation

The cylindrical surface of the sample was smeared with a thin layer of silicone gel. Then, the shear blocks were encapsulated in a fluorinated ethylene propylene (FEP) heat-shrink tube. The shear assembly was placed into a confining cell, and then two pistons of the confining cell were connected with the shear blocks via two collars to restrict sliding along their contact surface. The shear assembly connected to the flow system was vacuumed for 1 h.

(2) Confining pressure loading

After the shear assembly was installed, confining pressure was exerted at a rate of 0.005 MPa/s.

(3) Pore fluid injection and equilibrium

The pore fluid was injected into the sample and maintained at a desired pressure until the test was finished. Pore fluid was injected into the sample through a syringe pump (ISCO, USA) from the inlet until the differential pressure between the inlet and the outlet and the flow rate of the ISCO pump both reached zero for the transient method. For the constant-pressure method, water was injected at the inlet, and the outlet was opened.

(4) Shear-flow test

The constant displacement mode of the true triaxial machine was used to shear the fracture, and shear displacement rates of 0.3 mm/min were adopted in this work. When the shear displacement stabilized at the desired valve, the transient method or the constant-pressure method was adopted to measure the permeability.

## 2.2 Experimental Results

In this study, the permeability of intact granite samples was measured, and the permeability evolution of the fractured samples was also monitored under different normal stress conditions. The mechanical and permeability data of the fractured samples were obtained simultaneously during the shear process.

The permeability of the intact samples was measured at effective stresses of 5 MPa and 10 MPa, resulting in permeability values of 3.51 $e^{-18}$ $m^2$ and 1.72 $e^{-18}$ $m^2$ (1 μD = 1 $e^{-3}$ mD = 1 $e^{-6}$ D = 1 $e^{-18}$ $m^2$), respectively. Figure 3 shows

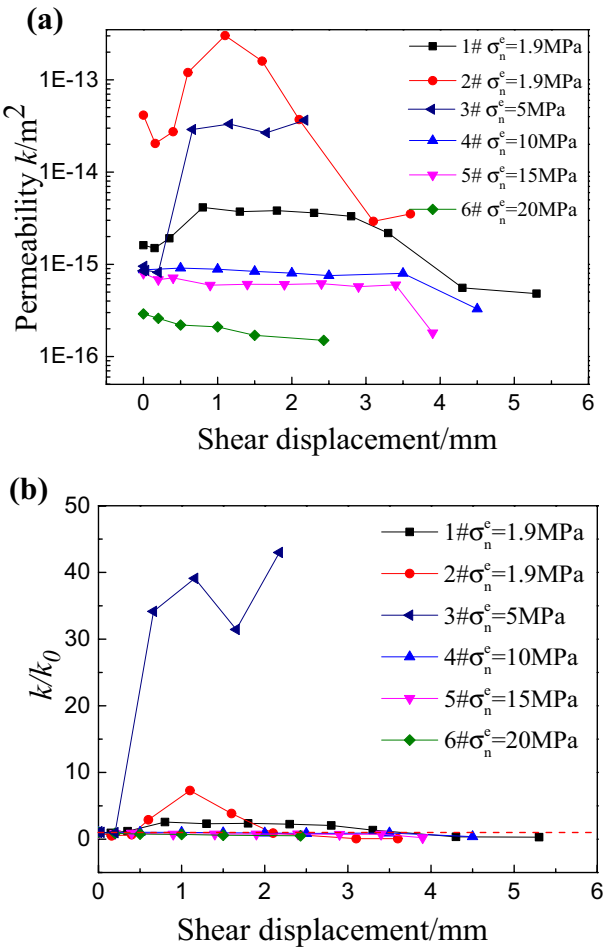


**Fig. 3** The dynamic permeability evolution of fractures with the shear displacement under different normal stresses. **a** The absolute permeability evolution, $k$. **b** The evolution relative to the initial permeability $k/k_0$

the dynamic permeability evolution of fractures with shear displacement under different normal stresses. As shown in Fig. 3a, the initial permeability of the fractures ranged from $10^{-12}$ to $10^{-16}$ $m^2$, which were significantly greater than that of the intact sample. The shear process markedly changed the permeability of the fractures under different normal stresses, and the variation trend of the permeability

under lower effective normal stresses ($\sigma_n^e \leq 5$ MPa) was obviously different from that under higher effective normal stresses ($\sigma_n^e > 5$ MPa). Under a low effective normal stress (1.9 MPa or 5 MPa), the permeability first decreased with shear displacement and then significantly increased. As the shear displacement continued to increase, the permeability was remarkably reduced until becoming lower than the initial permeability. Under a high effective normal stress (10–20 MPa), generally, the fracture permeability continuously decreased with the shear displacement. As shown in Fig. 3b, the permeability evolution relative to the initial permeability ($k/k_0$) is closely related to the effective normal stress. When the effective normal stress was greater than 5 MPa, $k/k_0$ was less than 1, i.e., the permeability decreased with increasing shear displacements. However, when the effective normal stress was not more than 5 MPa, shear displacement could enhance the permeability.

The initial permeability of the fracture decreased with increasing normal stress, although different samples had different permeability values under the same normal stress, such as the results of samples #1 and #2 under a normal stress of 2 MPa.

Figure 4 shows the curves of the permeability and the shear stress of the fractures versus the shear displacement. The curves of the shear stress versus the shear displacement exhibit a similar characteristic in that the fractures all experience three stages, including stage I, elastic deformation; stage II, the transition stage; and stage III, shear sliding (Xia Caichu 2002). In stage I, elastic deformation, the shear stress increases rapidly with the shear displacement, and the relationship between these values is linear. Stage II, the transition stage, is the transition between the elastic zone and the plastic sliding zone. In stage III, shear slipping, the shear stress changes little, but the shear displacement is large. These three stages are related to the shearing mechanism, and the acoustic emissions (AE) counts showed obvious differences between these stages. In stage I, the AE count was relatively low and slowly increased. In stage II, the AE count increased dramatically and reached the maximum when the major asperities were cut off. In stage III, the AE count reached the minimum, and sliding of the joint surface was the primary movement during this period (Wang et al. 2016). The stages with increasing permeability values under low effective normal stress (1.9 MPa and 5 MPa) were generally stages I and II. The fracture permeability was enlarged by an order of magnitude in stages I and II, with a weak drop in the early stages. In stage III, regardless of the effective normal stress, the fracture permeability consistently declined.

Figure 5 shows the curves of the changes in the normal deformation and permeability relative to the shear displacement. For the normal deformation of the fracture, the convention is adopted in which compression is negative and dilation is positive. As shown in Fig. 5, the normal deformation changed only slightly or experienced weak compression during the initial stage. Then, the normal deformation was significant dilation. The permeability decreased with the shear displacement when the fracture was compressed. When the fracture was dilated, the variation in the permeability was related to not only the normal deformation but also the normal stress magnitude. Under a lower normal stress ($\sigma_n^e \leq 5$ MPa), the permeability first increased with the shear displacement and then decreased. Under a higher normal stress ($\sigma_n^e > 5$ MPa), the permeability mainly decreased with the shear displacement.

Figure 6 shows the sheared samples. Because the confining oil leaked into sample #6 at the end of the shear test, sheared sample #6 is not shown in Fig. 6. A number of loose particles are observed, which are mainly the sheared asperities. The size of the particles decreased while the amount of the particles increased with increasing normal stress. The slickened lines on the fracture surface due to shear slipping were more obvious under high-normal stress conditions than under low-normal stress conditions.

## 3 DEM Shearing Tests on Fractured Samples

To understand the relationship between the shear mechanism and the dynamic permeability evolution, the shearing process of fractured rocks was simulated and analysed based on DEM. The main mineral components of the studied granite were quartz and feldspar, and the mechanical properties of these minerals are not sensitive to the presence of water (Jaeger et al. 2009). In addition, effective normal stress is suitable for this fractured rock (Rutter and Hackston 2017). Thus, effective normal stress was adopted in the numerical models, and the effects of the pore fluid on the mechanism were ignored in the shearing process.

### 3.1 Numerical Model

#### 3.1.1 Model Setup

In DEM, the bond-removal method (Asadi et al. 2013a; Cundall 2000; Park and Song 2013) and the addition of a smooth-joint model (Lambert et al. 2010) are the most common methods used to simulate fractures. However, with the bond-removal method, it is hard to reproduce the sliding behaviour of planar joints. With the abovementioned two numerical methods, the curve of the shear stress versus the shear displacement is unrealistic, because the shear stress is approximately constant post peak for a planar fracture in an actual test. In contrast, with the bond-removal method, the shear stress first reaches the peak stress and then decreases, and with the smooth-joint model, the shear stress increases

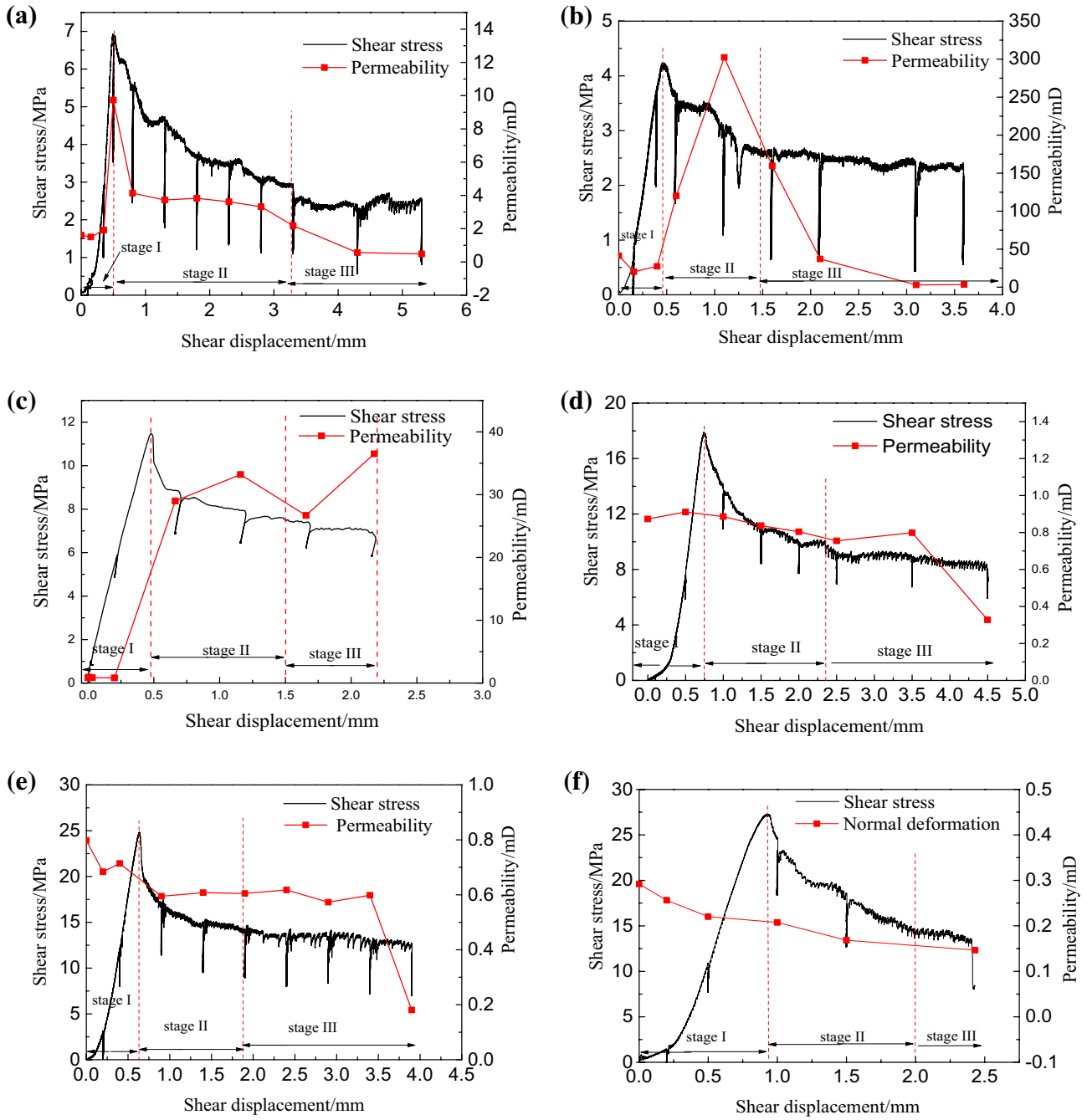


**Fig. 4** The curves of the variations in the shear stress and permeability with the shear displacement: **a** and **b** samples #1 and #2 at $\sigma_n^e$= 1.9 MPa; **c** sample #3 at $\sigma_n^e$ = 5 MPa; **d** sample #4 at $\sigma_n^e$ = 10 MPa; **e** sample #5 at $\sigma_n^e$ = 15 MPa; and **f** sample #6 at $\sigma_n^e$ = 20 MPa

again when the shear displacement exceeds the particle size. Both types of results are produced based on the interlocking particles (Bahaaddini et al. 2013). To overcome the shortcomings of these methods, Bahaaddini et al. (2013) proposed a new shear box genesis approach to study the shear behaviours of joints. This approach effectively reproduces the shear process of a fracture. It is conductive to studying the mechanical behaviours of fractures under different normal stress conditions. In this work, the approach approved by Bahaaddini et al. (2013) was used to analyse the evolution of the fracture permeability during shearing.

The rock sample was generated as the upper and lower blocks, as shown in Fig. 7. The upper and lower boxes were separately created, and each had four walls. The shapes of the rough walls between the two blocks coincided with the fracture traces of the physical rocks studied. It is noted that

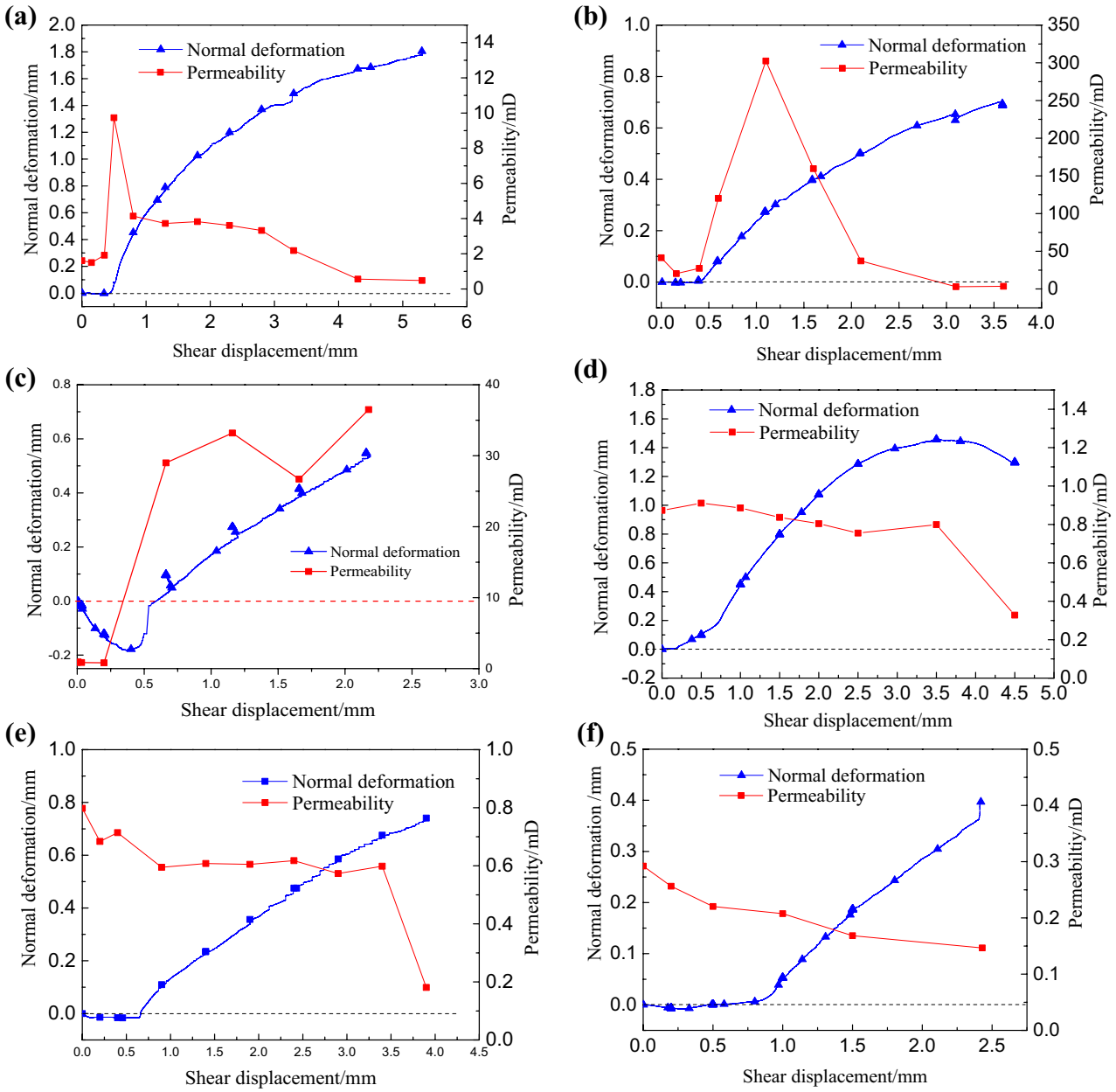


**Fig. 5** The curves of the variations in the normal deformation and permeability with the shear displacement: **a** and **b** samples #1 and #2 at $\sigma_n^e$= 1.9 MPa; **c** sample #3 at $\sigma_n^e$ = 5 MPa; **d** sample #4 at $\sigma_n^e$ = 10 MPa; **e** sample #5 at $\sigma_n^e$ = 15 MPa; and **f** sample #6 at $\sigma_n^e$ = 20 MPa

the surface of the fracture was scanned using a laser scanner, and the profile along the axial direction in the middle of surface was chosen as the representative roughness profile for the 2D simulation. Because this model is 2D, only one profile was represented in the fracture. When the particles were densely packed into the two boxes, the particles of each block were bonded with parallel bonds. Next, the rough walls were removed, and a normal stress was applied to the upper block. Many newly unbonded contacts were generated between the two blocks, and the contact model of these newly bonded contacts was achieved using the smooth-joint model. The orientation of each smooth-joint contact was perpendicular to the trace of the fracture.

The length and height of each numerical sample were 70 mm and 38 mm, respectively, and were the same as those of the physical samples, as shown in Fig. 7. In this work, the shortest line forming the roughness profile was about 0.5 mm. The size of the particles needed to be smaller than this value to simulate the asperities. Meanwhile, in a model, the number of particles increased with the decrease in the particle size, inducing a sharp increase in the computation time. Thus, considering the

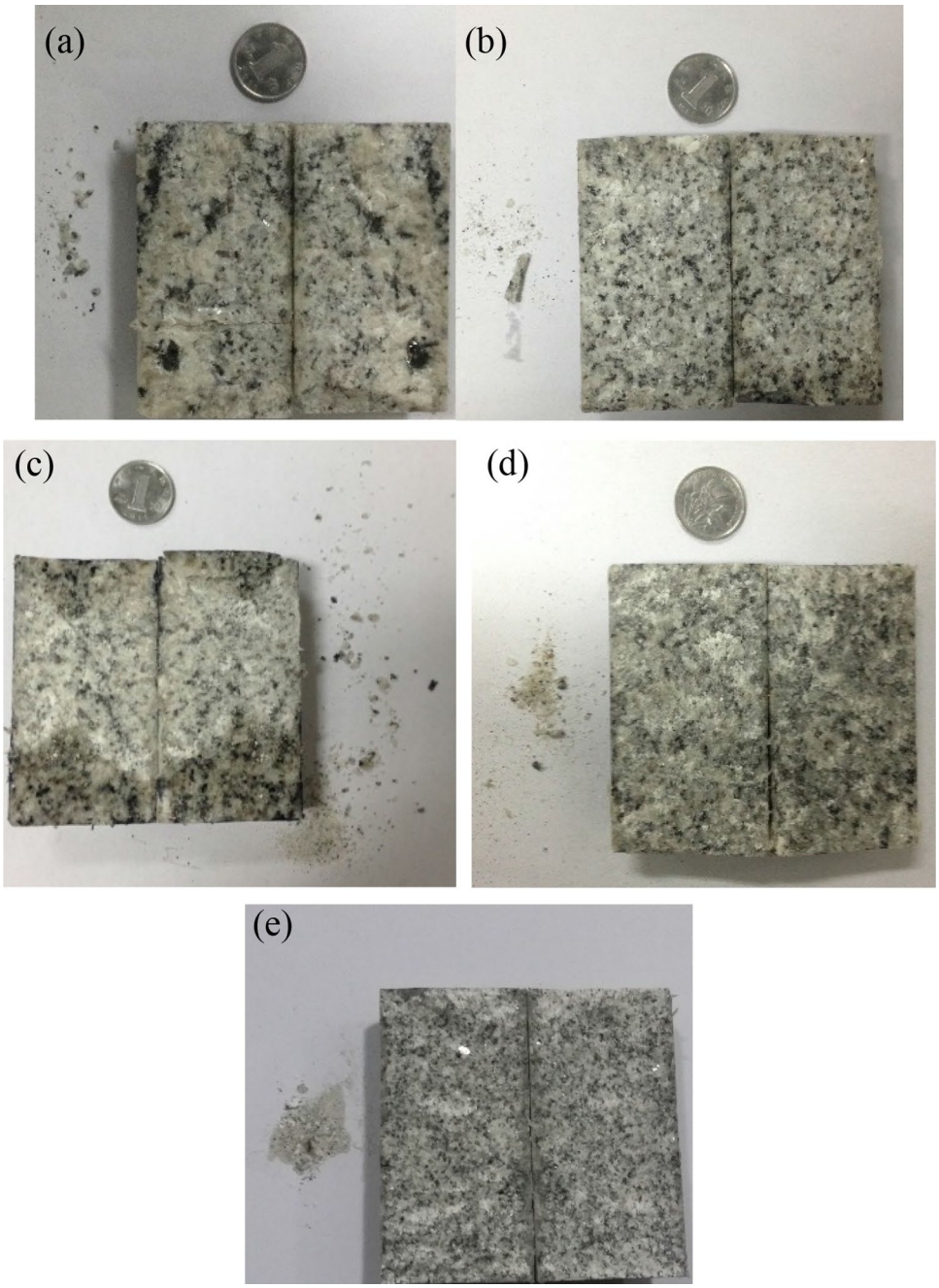


**Fig. 6** The sheared samples: **a** and **b** samples #1 and #2 at $\sigma_n^e = 1.9$ MPa; **c** sample #3 at $\sigma_n^e = 5$ MPa; **d** sample #4 at $\sigma_n^e = 10$ MPa; and **e** sample #5 at $\sigma_n^e = 15$ MPa

computational efficiency, the particle radii were uniformly distributed from 0.11 to 0.183 mm. Each sample contained approximately 34,222 particles. During the shearing process, first, the normal stress was applied to the upper wall and kept constant. Then, the lower block was restrained, but the upper block was set to a horizontal velocity of 0.2 m/s for shearing. The time step in each numerical model was $3 \times 10^{-9}$ s. Thus, the shear rate was approximately $6.0 \times 10^{-10}$ m/time step. A preliminary study proved that this rate is small enough to ensure the stability of the confining pressure and that the system remains under quasi-static loading.

#### 3.1.2 Smooth-Joint Model

The core of DEM is the contact model, which determines the mechanical behaviours of the particles. Thus, in the smooth-joint model, the model of the contact between particles on opposite sides of the fracture controls the shear behaviour. As shown in Fig. 8, when a smooth joint was created within the rock sample, surface 1 and surface 2 formed the joint

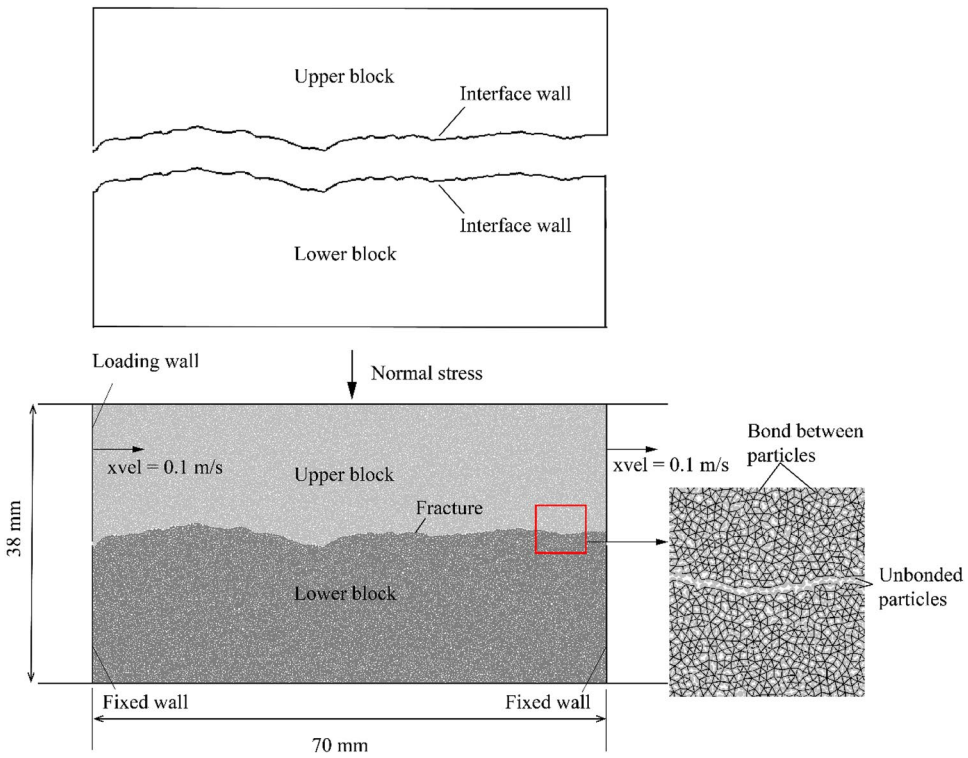


**Fig. 7** Numerical model of the direct shear test

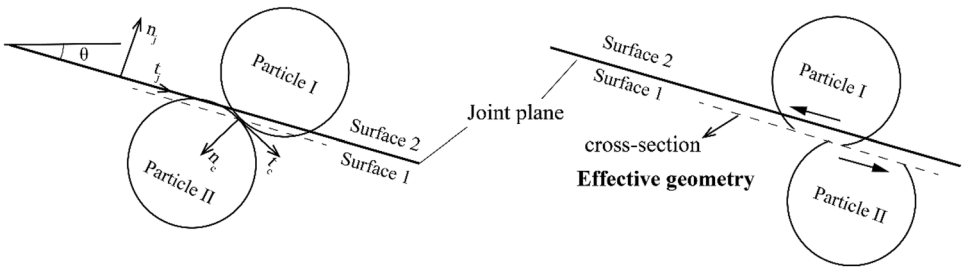


**Fig. 8** The behaviour of smooth-joint contact (modified from Potyondy and Cundall 2004)

plane. The relative particles could pass through each other along the joint plane and were not forced to move around one other. The unit normal vectors $\boldsymbol{n_j}$ and $\boldsymbol{n_c}$ indicate the orientation of the joint and contact, respectively. The dot product of $\boldsymbol{n_c}$ and $\boldsymbol{n_j}$ indicates the surface that each particle lies along. If $\boldsymbol{n_c} \cdot \boldsymbol{n_j} \geq 0$, the particle lies along surface 1 (Itasca Consulting Group 2014). The contact force $\boldsymbol{F}$ and the relative displacement $\boldsymbol{U}$ are resolved into normal and shear components by considering the orientation of the joint:

$$F = F_n \cdot \boldsymbol{n_j} + \boldsymbol{F_s}, \tag{3}$$

$$U = U_n \cdot \boldsymbol{n_j} + \boldsymbol{U_s}. \tag{4}$$

Here, the subscripts n and s indicate normal and shear in the local coordinate system of the joint plane, respectively.

In DEM, the force–displacement law, which is defined by the contact model, determines the behaviour of particles. In the smooth-joint model, the relationship between the unbonded contacts is shown in Fig. 9. A smooth contact can be assumed to have a circular cross-section, in which elastic springs are uniformly distributed. The area of this cross-section is calculated as follows:

$$A = \Pi R^2, \tag{5}$$

$$\text{with } R = \lambda \min\left(R_1, R_2\right), \tag{6}$$

where $R_1$ and $R_2$ are the radii of particle I and particle II, respectively. $\lambda$ is the radius multiplier, which is usually equal to 1.0.

The normal stiffness $k_n$, shear stiffness $k_s$, coefficient of friction μ and dilation angle $\psi$ are the key parameters controlling the mechanical behaviour of the smooth-joint contacts. The normal force $F_n$ is linearly proportional to $k_n$:

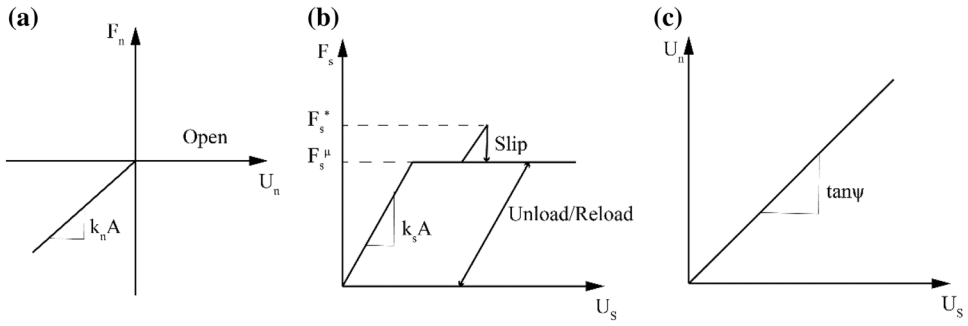


**Fig. 9** Force–displacement laws of an unbonded contact. **a** Normal force versus normal displacement, **b** shear force versus shear displacement, and **c** normal displacement versus shear displacement during sliding (modified from Itasca Consulting Group 2014)

$$F_{\mathrm{n}} = F_{\mathrm{n}} + k_{\mathrm{n}} A \Delta U_{\mathrm{n}}, \tag{7}$$

where $\Delta U_{\mathrm{n}}$ is the increment of the normal displacement in a time step.

The value of the shear strength $F_{\mathrm{s}}^{\mu}$ depends on the normal force $F_{\mathrm{n}}$:

$$F_{\mathrm{s}}^{\mu} = \mu F_{\mathrm{n}}. \tag{8}$$

A virtual force $||F_{\mathrm{s}}^{*}||$ used to infer the shear force and is calculated as follows:

$$||F_{\mathrm{s}}^{*}|| = \left|\left|F_{\mathrm{s}} + k_{\mathrm{s}} A \Delta U_{\mathrm{s}}\right|\right|. \tag{9}$$

If $||F_{\mathrm{s}}^{*}|| \le F_{\mathrm{s}}^{\mu}$, then the shear force $F_{\mathrm{s}}$ is

$$F_{\mathrm{s}} = F_{\mathrm{s}}^{*}. \tag{10}$$

Otherwise, if the particle does not slip:

$$F_{\mathrm{s}} = F_{\mathrm{s}}^{\mu}(F_{\mathrm{s}}^{*}/||F_{\mathrm{s}}^{*}||), \tag{11}$$

and if the particle is sliding, the normal force $F_{\mathrm{n}}$ and shear force $F_{\mathrm{s}}$ are updated as follows:

$$||F_{\mathrm{s}}|| = F_{\mathrm{s}}^{\mu *}, \tag{12}$$

$$F_{\mathrm{n}} = F_{\mathrm{n}} + \left(\frac{|F_{\mathrm{s}}^{*}| - F_{\mathrm{s}}^{\mu}}{k_{\mathrm{s}}}\right) k_{\mathrm{n}} A \tan\psi. \tag{13}$$

## 3.2 Calibration of Micro-scale Parameters

There is no definite relationship between the micro-parameters used and the macro-properties of the rock. Therefore, the micro-parameters should be calibrated by comparing the mechanical behaviour of the numerical model with that of the physical rock (Potyondy and Cundall 2004). In this work, the calibration of the micro-parameters was undertaken in two steps. First, the parameters of the parallel contact model were calibrated against a uniaxial compressive property. A uniaxial compression experiment on an intact rock was used to calibrate the micro-parameters of the parallel contact model. In the numerical model, a series of particles were bonded by parallel-bond contacts to simulate an intact sample. The scale of the numerical sample was the same as that of the physical experiments: 38 mm wide and 70 mm high. The micro-parameters used in this model are listed in Table 4. The mechanical parameters of the numerical model are in good agreement with those of the physical rock, as shown in Table 5.

**Table 4** Micro-parameters of the particles and bonds

| Parameter | Value |
|---|---|
| Density of particles, $\rho$ (kg/m$^3$) | 2205 |
| Minimum particle radius, $r_{\mathrm{min}}$ (mm) | 0.12 |
| Maximum particle radius, $r_{\mathrm{max}}$ (mm) | 0.1992 |
| Effective modulus of both the particles and bond, $E_{\mathrm{c}}$ (GPa) | 17.4 |
| Ratio of the normal to shear stiffness of both the particles and bond, $k_{\mathrm{n}}/k_{\mathrm{s}}$ | 1.9 |
| Tensile strength of the bond, $\sigma_{\mathrm{b}}$ (MPa) | 56 |
| Cohesion strength of the bond, $c_{\mathrm{b}}$ (MPa) | 56 |
| Local friction angle, $\phi_{\mathrm{b}}$ (°) | 30 |

**Table 5** The mechanical parameters of the numerical model and physical rock under uniaxial loading

| Object of study | Young's modulus (GPa) | Poisson's ratio (1) | Uniaxial strength (MPa) |
|---|---|---|---|
| Numerical model | 36.85 | 0.225 | 184.29 |
| Physical rock | 36.72 | 0.226 | 184.91 |

Second, the shear stresses of the physical fractured samples were used to calibrate the parameters of the smooth joint contacts. Because the effective normal stress applied to samples #1 and #2 was the same, sample #2 was not simulated. Five numerical samples (1#, 3#–6#) were generated in the simulation, and the fracture trace of each numerical sample was the middle profile of the corresponding physical sample. As shown in Fig. 10a, the peak shear strengths of the numerical samples were close to those observed from the physical experiments. As the normal stress increased,

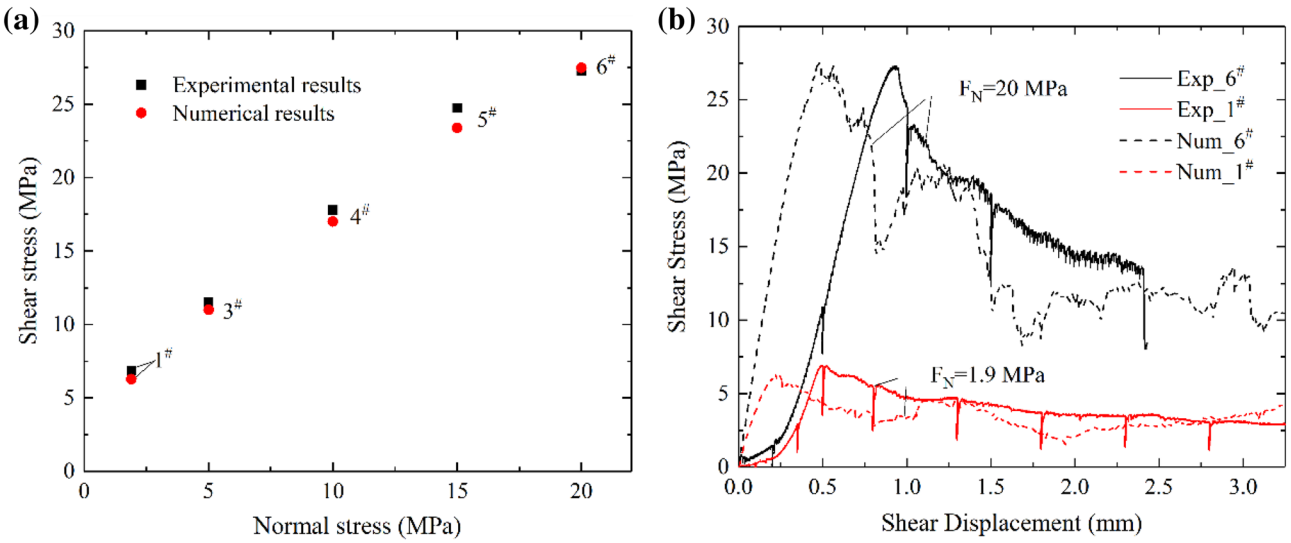


**Fig. 10** Comparison of the numerical and experimental results. **a** The peak shear strength envelopes of the numerical and experimental tests. **b** Shear stress versus shear displacement

**Table 6** The calibrated parameters of the smooth-joint model

| Parameter | Value |
|---|---|
| SJ normal stiffness (GPa/m) | 280 |
| SJ shear stiffness (GPa/m) | 120 |
| SJ coefficient of friction | 3.0 |

the peak shear strength also increased. In addition, Fig. 10b shows that the shear stress versus shear displacement curves of the numerical model agree well with those of the experiment. Although the experimental curve exhibits a compaction stage, this stage does not exist in the numerical model. This is because the particles are densely packed into the initial numerical samples. It is noted that the shear stress increased as the shear displacement increased. After the peak stress was reached, the shear stress decreased. The shear behaviour can be well presented by the numerical model. Under different normal stresses, both the shear stress–strain curve and the changes of the peak show that the numerical results are in good agreement with the results of the physical experiments. Therefore, the parameters used in the smooth joint model are suitable for fracture simulation. The calibrated parameters are shown in Table 6.

## 3.3 Numerical Results

### 3.3.1 Effects of Normal Stresses on the Matched Fractures

To understand the effect of normal stresses on the matched fractures, all five numerical samples were compressed under normal stresses ranging from 1.9 to 20 MPa. It was obvious that in the numerical model, although the boundary of the upper block matched that of the lower block, some gaps existed in adjacent particles between the upper and lower blocks, as shown in Fig. 11b. This is because the shape of particles was circular, and the boundary influences the distribution of particles along the fractures. In the numerical model, a smooth-joint contact becomes active only when the gap between the particles is less than or equal to 0. The presence of active contacts in the numerical model indicates that the corresponding particles overlap at these contacts. Additionally, the overlapping of particles indicates the closing of the fracture at that position. Thus, in the initial samples, only part of the fracture was closed (in contact). The existence of the gaps is also reasonable in the physical samples. When an intact sample was split, there was always some damage on the failure surface, and some particles fell from the rock. These types of damage formed small channels, which made it possible for fluid to flow through the fracture. This is also a reason why the permeability of fractured rock is much higher than that of intact rock.

The effective contact area between the blocks, which is defined as the sum of the areas of active smooth-joint contacts, reflects the closed part of the fracture, as shown in Fig. 11. In the 2D model, the fracture was simply a line. However, the fracture was a rough surface in the physical sample. The dispersed and unclosed parts of the fracture surface could be connected to form channels for fluid flow. Thus, the effective contact area can reflect the fracture unconnectedness. A greater amount of effective contact area indicates more closed parts, inducing inferior connectivity of the fracture, and vice versa. It is obvious that many contacts in the fracture changed from inactive to active as the

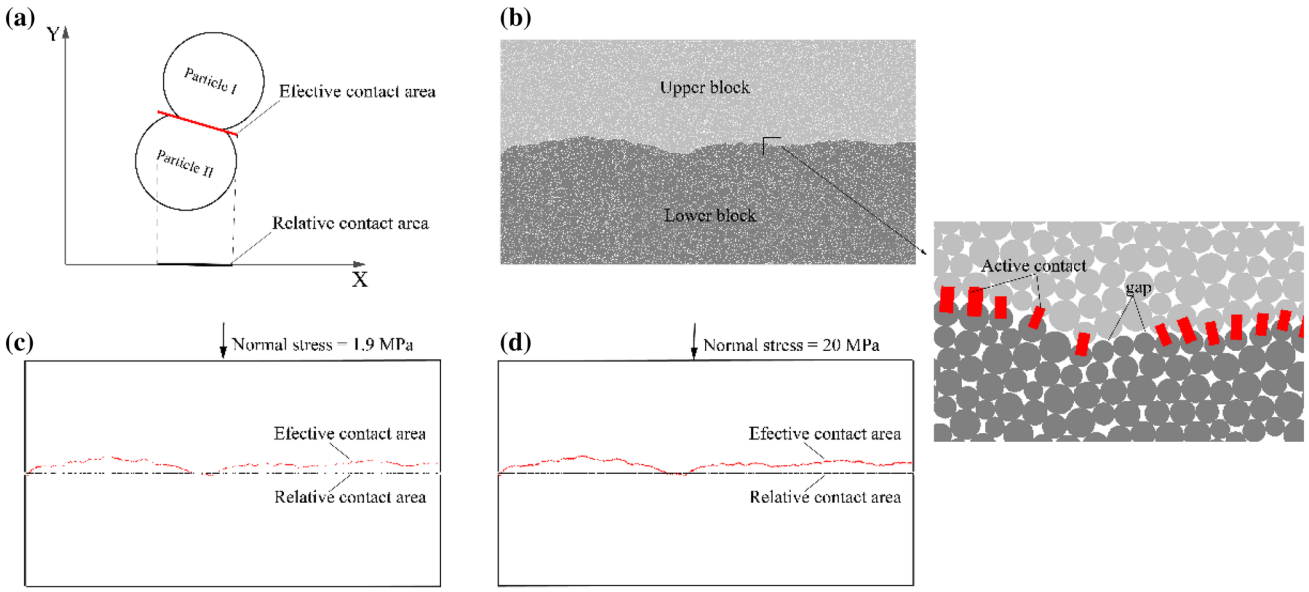


**Fig. 11** Effect of normal stress on the contact area. **a** Definitions of the effective contact area and relative contact area; **b** configuration of model #6; **c** contact area of the model under 1.9 MPa of normal stress; and **d** contact area of the model under 20 MPa of normal stress

normal stress increased so that the effective contact area increased (Fig. 11c, d). That means that many opened parts were closed under the action of the normal stress. It is noted that the fracture traces of the five samples were different. Therefore, it is difficult to directly compare the effective contact areas of the five samples. To facilitate comparison of the five samples, the relative contact area Ar (mm), which is defined as the projection of the effective contact area, is put forward, as shown in Fig. 11a. The calculation of the relative contact area was undertaken in two steps. First, the area of every active contact was projected onto the *X*-axis. Then, the sum of the projected areas was calculated. If several adjacent contact projections overlapped, the overlapping area was calculated only once. For the matched fractures, Fig. 11c, d show that the active contacts were always distributed randomly along the fracture as the normal stress increased. Therefore, the relative contact area can also be used to evaluate the connectivity of a matched fracture.

Analysing the effect of normal stresses on the relative contact area provides a great way to explain why the initial permeability of the fracture decreased with increasing normal stress in the physical experiment (Fig. 3a). Figure 12 shows the effect of normal stresses on the relative contact area. Under the same normal stress, these samples had almost equivalent relative contact areas. The slight differences resulted from the different fracture traces. As the normal stress increased, the relative contact area of each sample increased sharply at first. When most of the whole fracture was closed, the relative contact area increased slowly. This is because a greater number of active contacts induces a higher normal stiffness of the fracture. A normal deformation large

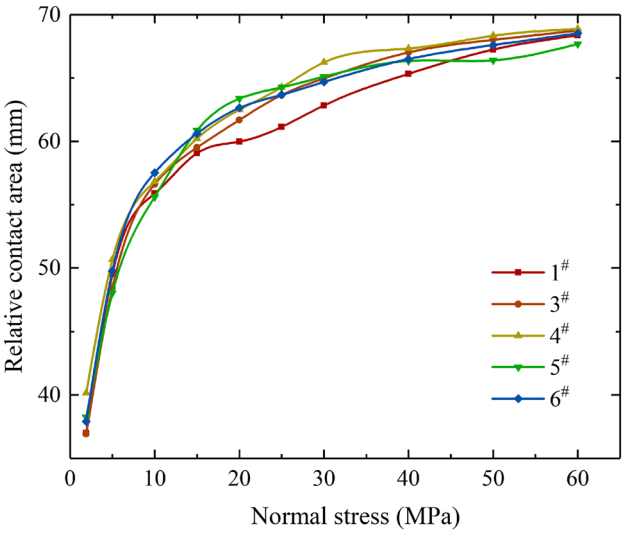


**Fig. 12** Effect of the normal stress on the relative contact area

enough to generate new active contacts requires a higher normal stress at this time. In general, the relative contact area increased as the normal stress increased, decreasing the permeability of the fracture.

### 3.3.2 Results of the Numerical Shear Test

The direct shear tests of five samples under different normal stresses were calibrated as shown in Fig. 10. The normal stress applied to sample #1 was 1.9 MPa, whereas 20 MPa was applied to sample #6. Figures 13 and 14 show the

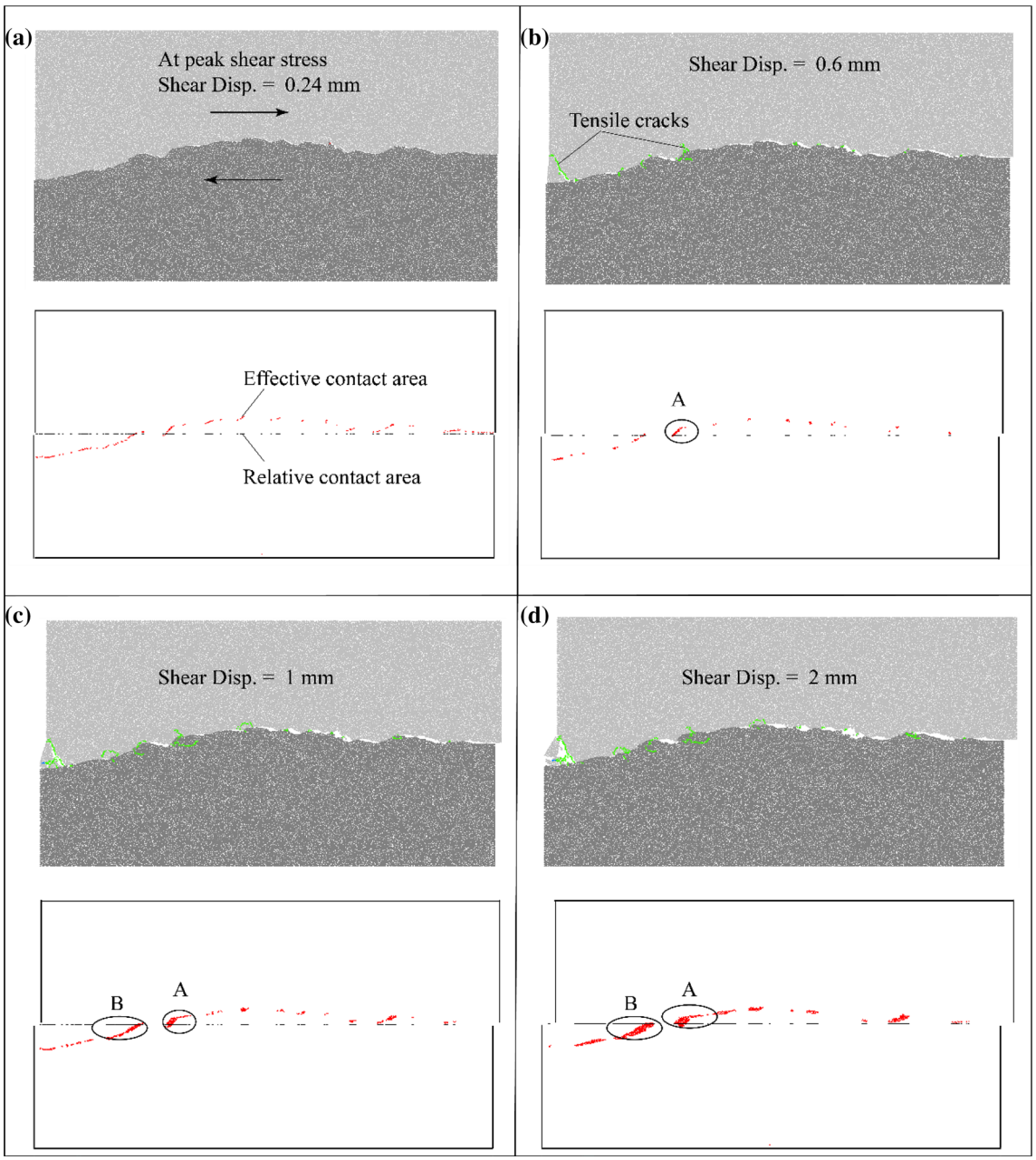


**Fig. 13** The propagation of cracks and the contact area of sample 1# during shear tests under 1.9 MPa normal stress. (For the cracks, green indicates tensile cracks, and blue indicates shear cracks. For the contact area, the red line represents the effective contact area, and the black line is the relative contact area)

propagation of cracks and the contact area of the two samples. When the contact force of a bond exceeded the bond strength, the bond was removed, and a crack was created. If the bond was broken by a tensile (shear) force, the crack was called a tensile (shear) crack. With increasing shear displacements, the crack numbers and the evolution of the relative contact areas between the two samples became clearly different (see Fig. 15).

For sample #1, the initial relative contact area was approximately 30 mm, accounting for 42.9% of the length of the rock sample. When the upper block slid along the fracture, the fracture boundary of the upper block no longer coincided with that of the lower block. Thus, the relative contact area began to decrease, as shown in Figs. 13a and 15a. Figure 13a also shows that no crack formed in sample #1 before the peak shear stress, indicating that the shearing mechanism was purely sliding at this stage. After the peak

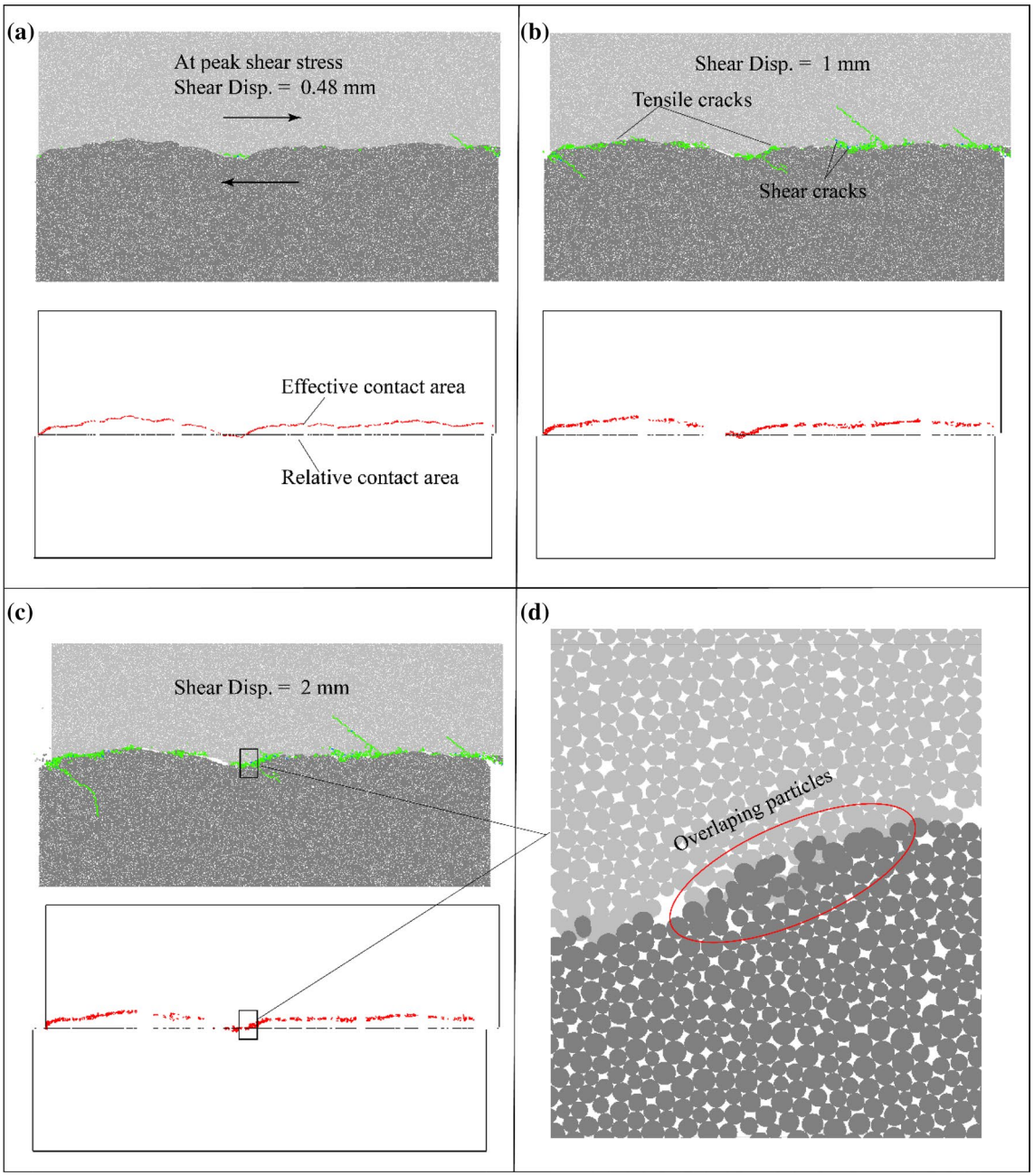


**Fig. 14** The propagation of cracks and the contact area of sample #6 during shear tests under 5.0 MPa of normal stress. (For the cracks, green indicates tensile cracks, and blue indicates shear cracks. For the contact area, the red line represents the effective contact area, and the black line is the relative contact area)

shear stress was reached, the relative contact area further decreased before the shear displacement reached 0.6 mm. The lowest relative contact area was approximately 10 mm, which accounted for 14.3% of the length of the rock sample. Additionally, it is obvious that the active smooth contacts were generally distributed at asperities (Fig. 13b). Therefore, the normal stress and shear stress concentrate on asperities, causing many cracks to form near asperities. The occurrence of cracks indicates that asperities are sheared off and that the shear mechanism is not only sliding but also shearing. When the shear displacement exceeded 0.6 mm, the relative contact area increased sharply, as shown in Fig. 15a. Because these new active contacts were around the sheared asperities, the relative contact area increased, and the effective contact area could be regarded as the area of the worn fracture (Fig. 13c). Notably, many new active smooth contacts were assembled in small areas, such as areas A and B in Fig. 13c, d. This was a result of the overlapping of many

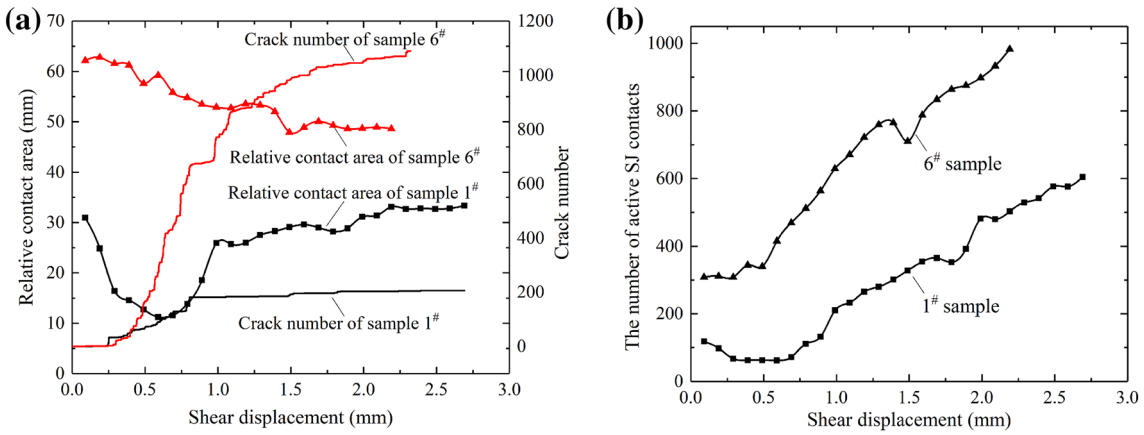


**Fig. 15** Results of the numerical shear tests on sample #1 and sample #6. **a** The relative contact area and crack number versus the shear displacement. **b** The number of active smooth-joint contacts versus the shear displacement

particles at these worn asperities, as shown in Fig. 14c. The overlapping of these particles can indicate that the sheared particles were further compacted as the shear displacement increased, as shown in Fig. 14d.

For sample #6, the initial relative contact area was over 80% of the fracture under 20 MPa of normal stress. Both shearing and sliding almost occurred during the shear test. At the beginning of the shear test, there were few cracks, and the relative contact area did not decrease. When the shear displacement exceeded 0.25 mm, many cracks were formed, and it was obvious that the relative contact area continuously decreased. This is because almost all the contacts at the asperities were active initially, and after the sliding of the upper block, the boundary of the upper block did not exactly match that of the lower block. It is worth noting that the contact area in sample #6 was always much larger than that in sample #1 during the shear test. Additionally, it can be determined that the crack number of sample #6 was much greater than that of #1 (Fig. 15). The cracks were also fully distributed near these active contacts. Thus, all of the contact area was worn away. The worn area in sample 6# was much bigger than that in sample 1#. Especially, these sheared off particles, which could be regarded as wear products, were always compacted by a high normal stress, inducing the appearance of new smooth joints, as the overlapping particles show in Fig. 14d.

Because many of the asperities were sheared off and compacted, the asperities were degraded. The number of active smooth joint contacts (SJ number) was recorded during the shear test to analyse the asperity degradation, as shown in Fig. 15b. For sample #1, the SJ number decreased during the purely sliding stage; however, the SJ number increased due to asperity degradation. Clearly, the SJ number of sample #6 continuously increased, even when the relative contact area decreased. This is because the sheared off particles were densely compacted. A greater SJ number indicates stronger degradation.

## 4 Discussion

Shearing process significantly affects the permeability of a rough granite fracture, and the variation trend of the permeability depends on the magnitude of the normal stress. The normal stress influences the permeability, including the initial permeability of the fracture without shearing and the variation trend of the fracture permeability during shearing. When no shear slipping occurs, the fracture aperture depends on the effective normal stress (Zhang et al. 2018), which determines the fracture permeability (Witherspoon et al. 1980). This work proved that the connectivity of matched fractures is affected by the effective normal stress, as shown in Fig. 12. The changes of the connectivity also play an important role in affecting the permeability. In the shearing process, the normal stress is a key factor that influences the aperture of a fracture, as shown in Fig. 16. Though normal deformation of the fractures occurs during shearing, the extent of expansion is related to the magnitude of the normal stress. With increasing normal stress, the extent of expansion decreases, i.e., a high normal stress will inhibit the increase in aperture during shearing. Therefore, fracture permeability is significantly affected by the normal stress in the shearing process. A high normal stress not only limits the dilatancy of the fracture but also enhances the formation of wear products, as shown in Fig. 6. Under a higher normal stress, more asperities are damaged and sheared off during the shearing process, as shown in Figs. 10 and 15.

The variation trend of the permeability is closely related to the normal stress, which dominates the shear mechanism. When the sample is compacted by a low normal stress,

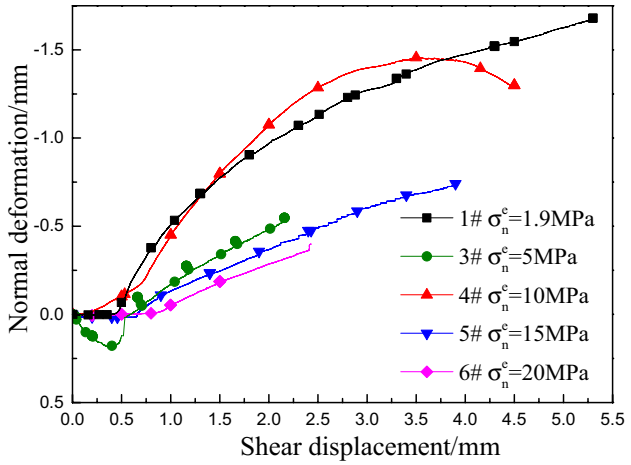


**Fig. 16** Normal deformation of the fractures with the shear distance under different normal stresses

it is obvious that the SJ number decreases first and then increases, while the trend of the permeability is reversed. The decrease of the SJ number is caused by the decrease of the relative contact area, which results from the pure sliding mechanism. The decrease of the closed part of the fracture is beneficial for building flow channels, resulting in increased permeability. When the shearing mechanism occurs, the SJ number increases. This results from asperity degradation. On the one hand, asperity degradation induces the increase of the relative contact area. On the other hand, damaged asperities can be compacted normal stress. These two effects induce poor fracture connectivity and decrease the permeability. The abovementioned reasons caused the permeability of samples #1 and #2 to first increase and later decrease during the shear test.

For a fracture under a high normal stress, the effective contact area is always very large in shear testing, inducing poor connectivity. Additionally, because of the high normal stress, the asperity degradation of the fracture is great, resulting in more cracks in the blocks. This induces crack production and the creation of more wear products. These wear products are densely compacted, as shown by the increase of the SJ number. Large wear products will impede the flow of fluid. The wear products can also migrate to adjacent pores by squeezing and rolling. For a sample under high normal stress, both the poor connection and the existence of many wear products are the reasons why the permeability continually decreases during shearing. In conclusion, the effect of the normal stress on the permeability evolution is realized by controlling the shear mechanism. Pure sliding will increase the connectivity and the permeability of a fracture, whereas shearing will induce asperity degradation and decrease the permeability of a fracture.

The evolution of the aperture during shearing results from the actions of the normal stress and the shear stress, and the influence of the shear stress is more complicated. Previous studies have suggested that shearing could either increase or decrease the permeability of a fracture. An increase in fracture permeability results from fracture dilatancy (Barton et al. 1985; Ishibashi et al. 2016), and a reduction in fracture permeability is caused by the formation of fault gouges (Fang et al. 2017, 2018; Faoro et al. 2009). In this study, the dilatancy of the fractures and the formation of fault gouges were shown to collectively change the fracture permeability. In stage I, before the shear stress reaches the peak stress, the fracture aperture changes slightly, and the asperities are hardly sheared off. The sliding mechanism plays a role in the shear process. Nonetheless, the fracture permeability must decrease if the aperture decreases. When the shear stress reaches the peak stress and then drops in stage II, asperities are sheared off, and the sheared particles are sandwiched between the fracture surfaces, which increases the fracture aperture. The influence of the dilatancy and the influence of the fault gouge begin to compete, i.e., to varying degrees, the sliding mechanism and the shearing mechanism begin working together in the shear process. The permeability evolution depends on the effective normal stress. In stage III, with increasing shear displacements, more asperities are sheared off, and the fracture surface becomes smoother than the initial state. The sheared asperities become finer and fill in the holes along the fracture surfaces. The sliding mechanism and the shearing mechanism are working together, as in stage II. Thus, the channels for fluid flow are obstructed by wear products, and the fracture permeability decreases.

Under different normal stresses, the mechanism of the permeability variations of fractures in granite has been qualitatively revealed through experiments and numerical simulations. It is meaningful to quantitatively and further analyse the competitive mechanism of the aperture and connectivity. Also, because it is difficult to obtain the evolution of the aperture and connectivity via experiments, three-dimensional simulations are needed, and the addition of fluids is also necessary in the future.

## 5 Conclusions

The dynamic permeability of a rough granite fracture was investigated using physical experiments and numerical models. The main findings are as follows:

1. As the effective normal stress increases, the fracture permeability decreases. When the normal stress increases, the effective contact area of the fracture increases. This change is not conducive to the establishment of flow channels.

2. Shear sliding significantly affects the permeability of a fracture, and the variation trend of the permeability depends on the magnitude of the effective normal stress. For a low effective normal stress, the fracture permeability decreases with the shear displacement in the first stage and then significantly increases. Under a high effective normal stress, the fracture permeability continuously decreases with the shear displacement.
3. The dilatancy of a fracture and the formation of fault gouges collectively influence the fracture permeability. Although fracture dilatancy occurs during shearing, the change in the permeability is not proportional to the normal deformation of the fracture sample.
4. The dynamic evolution of the permeability of a fracture is related to the shear mechanism. Under a low normal stress, only pure sliding behaviour is observed first, which increases the connectivity of the fracture, resulting in an increase in the permeability. As the shear displacement increases, the shearing behaviour degrades the roughness of the fracture. The connectivity decreases, and fault gouges form, decreasing the permeability. However, under a high normal stress, sliding and shearing both occur almost throughout the shear test. The high effective normal stress not only limits the dilatancy of the fracture but also enhances the formation of fault gouges. Thus, the fracture permeability still decreases during shear testing under a high normal stress.

**Acknowledgements** This research was supported by the National Key R&D Program of China (no. 2016YFB0600805), the Youth Fund of the National Natural Science Foundation of China (41702289) and the Open Research Fund of State Key Laboratory of Geomechanics and Geotechnical Engineering, Institute of Rock and Soil Mechanics, Chinese Academy of Sciences (no. Z017008).

## Compliance with Ethical Standards

**Conflict of interest** The authors declare that they have no conflicts of interest for this work.

## References

Amadei B, Illangasekare T (1994) A mathematical model for flow and solute transport in non-homogeneous rock fractures. Int J Rock Mech Min 31:719–731. https://doi.org/10.1016/0148-9062(94)90011-6

Asadi MS, Barla GJRM, Engineering R (2012) A bonded particle model simulation of shear strength and asperity degradation for rough rock fractures. Rock Mech Rock Eng 45:649–675

Asadi MS, Barla GJRM, Engineering R (2013a) A laboratory shear cell used for simulation of shear strength and asperity degradation of rough rock fractures. Rock Mech Rock Eng 46:683–699

Asadi MS, Rasouli V, Barla G (2013b) A laboratory shear cell used for simulation of shear strength and asperity degradation of rough rock fractures rock mechanics and rock engineering 46:683–699. https://doi.org/10.1007/s00603-012-0322-2

Bahaaddini M, Sharrock G, Hebblewhite BKJC (2013) Numerical direct shear tests to model the shear behaviour of rock joints. Geotechnics 51:101–115

Bahaaddini M, Hagan PC, Mitra R, Khosravi MH (2016) Experimental and numerical study of asperity degradation in the direct shear test. Eng Geol 204:41–52. https://doi.org/10.1016/j.enggeo.2016.01.018

Bart M, Shao JF, Lydzba D, Haji-Sotoudeh M (2004) Coupled hydro-mechanical modeling of rock fractures under normal stress. Can Geotech J 41:686–697. https://doi.org/10.1139/t04-018

Barton N, Bandis S, Bakhtar K (1985) Strength, deformation and conductivity coupling of rock joints. Int J Rock Mech Min Sci Geomech Abstr 3:121–140

Cundall PA (2000) Numerical experiments on rough joints in shear using a bonded particle model. In: Lehner FK, Urai JL (eds) Aspects of tectonic faulting: in honour of Georg Mandl. Springer, Berlin, pp 1–9. https://doi.org/10.1007/978-3-642-59617-9_1

Esaki T, Du S, Mitani Y, Ikusada K, Jing L (1999) Development of a shear-flow test apparatus and determination of coupled properties for a single rock joint. Int J Rock Mech Min Sci 36:641–650

Fang Y, Elsworth D, Wang C, Ishibashi T, Fitts JP (2017) Frictional stability-permeability relationships for fractures in shales. J Geophys Res Solid Earth 122:1760–1776

Fang Y, Elsworth D, Ishibashi T, Zhang FS (2018) Permeability evolution and frictional stability of fabricated fractures with specified roughness. J Geophys Res Sol Ea 123:9355–9375. https://doi.org/10.1029/2018jb016215

Faoro I, Niemeijer A, Marone C, Elsworth D (2009) Influence of shear and deviatoric stress on the evolution of permeability in fractured rock. J Geophys Res. https://doi.org/10.1029/2007jb005372

Gangyan GWJ, Yuding Y (1990) An experimental study of naturally cracked rock permeabilty. J Seismol Res 20:319–328

Giger S et al (2011) Design, operation and validation of a new fluid-sealed direct shear apparatus capable of monitoring fault-related fluid flow to large displacements. Int J Rock Mech Min Sci 48:1160–1172

Giwelli A et al (2016) Laboratory observations of fault transmissibility alteration in carbonate rock during direct shearing. Geofluids 16:658–672. https://doi.org/10.1111/gfl.12183

Huang J, Xu S, Hu S (2014) Numerical investigations of the dynamic shear behavior of rough rock joints. Rock Mech Rock Eng 47:1727–1743. https://doi.org/10.1007/s00603-013-0502-8

Ishibashi T, Watanabe N, Asanuma H, Tsuchiya N (2016) Linking microearthquakes to fracture permeability change: the role of surface roughness. Geophys Res Lett 43:7486–7493

Itasca Consulting Group l (2014) PFC (particle flow code in 2 and 3 dimensions), version 5.0 [User's manual]. Minneapolis

Jaeger JC, Cook NG, Zimmerman R (2009) Fundamentals of rock mechanics. Wiley, New York

Ji SH, Koh YK, Kuhlman KL, Lee MY, Choi JW (2013) Influence of pressure change during hydraulic tests on fracture aperture. Ground Water 51:298–304. https://doi.org/10.1111/j.1745-6584.2012.00968.x

Kamali-Asl A, Ghazanfari E, Perdrial N, Bredice N (2018) Experimental study of fracture response in granite specimens subjected to hydrothermal conditions relevant for enhanced geothermal systems. Geothermics 72:205–224. https://doi.org/10.1016/j.geothermics.2017.11.014

Lambert C, Buzzi O, Giacomini AJC (2010) Influence of calcium leaching on the mechanical behavior of a rock–mortar interface: a DEM analysis. Comput Geotech 37:258–266

Lang PS, Paluszny A, Zimmerman RW (2016) Evolution of fracture normal stiffness due to pressure dissolution and precipitation. Int J Rock Mech Min Sci 88:12–22. https://doi.org/10.1016/j.ijrmms.2016.06.004

Lee HS, Cho TF (2002) Hydraulic characteristics of rough fractures in linear flow under normal and shear load. Rock Mech Rock Eng 35:299–318. https://doi.org/10.1007/s00603-002-0028-y

Nishiyama S, Ohnishi Y, Ito H, Yano T (2014) Mechanical and hydraulic behavior of a rock fracture under shear deformation Earth. Planets Sp 66:108. https://doi.org/10.1186/1880-5981-66-108

Park J-W, Song J-J (2013) Numerical method for the determination of contact areas of a rock joint under normal and shear loads. Int J Rock Mech Min Sci 58:8–22. https://doi.org/10.1016/j.ijrmms.2012.10.001

Potyondy DO, Cundall PA (2004) A bonded-particle model for rock. Int J Rock Mech Min Sci 41:1329–1364

Rong G, Yang J, Cheng L, Zhou C (2016) Laboratory investigation of nonlinear flow characteristics in rough fractures during shear process. J Hydrol 541:1385–1394. https://doi.org/10.1016/j.jhydrol.2016.08.043

Rutter E, Hackston A (2017) On the effective stress law for rock-on-rock frictional sliding, and fault slip triggered by means of fluid injection. Philos Trans A Math Phys Eng Sci. https://doi.org/10.1098/rsta.2016.0001

Shu B, Zhu R, Tan J, Zhang S, Liang M (2019) Evolution of permeability in a single granite fracture at high temperature. Fuel 242:12–22. https://doi.org/10.1016/j.fuel.2019.01.031

Snow DT (1969) Anisotropie permeability of fractured media. Water Resour Res 5:1273–1289. https://doi.org/10.1029/WR005i006p01273

Stober I, Bucher K (2015) Hydraulic conductivity of fractured upper crust: insights from hydraulic tests in boreholes and fluid-rock interaction in crystalline basement rocks. Geofluids 15:161–178. https://doi.org/10.1111/gfl.12104

Takahashi M (2003) Permeability change during experimental fault smearing. J Geophys Res Solid Earth. https://doi.org/10.1029/2002jb001984

Wang GJY, Wang W, Li T (2009) Development and application of an improved numeric control shear-fluid coupled apparatus for rock joint. Rock Soil Mech 30:3200–3208. https://doi.org/10.16285/j.rsm.2009.10.049

Wang G, Zhang X, Jiang Y, Wu X, Wang S (2016) Rate-dependent mechanical behavior of rough rock joints. Int J Rock Mech Min Sci 83:231–240. https://doi.org/10.1016/j.ijrmms.2015.10.013

Witherspoon PA, Wang JSY, Iwai K, Gale JE (1980) Validity of cubic law for fluid flow in a deformable rock fracture. Water Resour Res 16:1016–1024. https://doi.org/10.1029/WR016i006p01016

Xia Caichu SZ (2002) Joint mechanics of engineering rock mass. Tongji University Press, Tongji

Yang Z, Lo S, Di C (2001) Reassessing the joint roughness coefficient (JRC) estimation using Z2. Rock Mech Rock Eng 34:243–251

Yang H, Xie S-Y, Secq J, Shao J-F (2017) Experimental study and modeling of hydromechanical behavior of concrete fracture. Water Sci Eng 10:97–106. https://doi.org/10.1016/j.wse.2017.06.002

Yeo IW, de Freitas MH, Zimmerman RW (1998) Effect of shear displacement on the aperture and permeability of a rock fracture. Int J Rock Mech Min Sci 35:1051–1070. https://doi.org/10.1016/s0148-9062(98)00165-x

Zhang Q, Li X, Bai B, Hu S, Shi L (2018) Effect of pore fluid pressure on the normal deformation of a matched granite. Jt Process. https://doi.org/10.3390/pr6080107